Université des Sciences et Technologies Lille 1
Universidad del Pais Vasco - Euskal Herriko Unibertsitatea
Master Thesis

Director: Prof. A. Rubio
Co-director: Dr. E. Cannuccia

Study of the Electronic Structure of hexagonal Boron Nitride on Metals Substrates

Paul Giraud

San Sebastian - Spain, September 20, 2012

Acknowledgments

There are many people I want to express my gratitude because they helped me, in a way or another, to achieve this present work.

My advisers, Angel Rubio and Elena Cannuccia, for their kindness and their guidance all along this project. My former teacher, Ludger Wirtz, who gave me the taste of Theoretical Physics and allowed my stay, here, in San Sebastian.

I also want to thank all the people I met in the Nano-Bio Spectroscopy or DIPC group, particularly people from my office, Mehdi, Kaike and Bruno. I will always remember the discussions we had about physics or whatsoever. I wish them all the best in their respective thesis. A special thank to David with whom we tried – sadly without success– to decipher that terrible Mahan's book:*Many particle Physics*! I do not forget Ask, who was kind enough to initiate me to the mysterious GPAW and Python code.

Finally, I would like to thank my old friends from Bayonne and Biarritz, they made me discover the Basque Country and its fabulous food and tradition. They even tried to teach me how to surf but after many attempts, I am rather doubtful about my skills at it.

Abstract

This thesis aims to investigate the effect of various metallic substrates (Nickel, Gold and Iridium) on the electronic properties of hexagonal–Boron Nitride (h-BN). The Angle Resolved Photoemission Spectroscopy (ARPES) data in pour possess highlight a modulation of the π band of h-BN depending on the substrates. We resorted to a combined ab-initio Density Functional Theory (DFT) study and a tight-binding model in order to simulate and characterize the relative surface state. We found that the substrates affects the relative position of the π band with respect to the Fermi level and its bandwidth.

Contents

List of Figures

List of Tables

Introduction

Since the first synthesization of graphene[1], a one atom-thick layer of graphite, the production of carbon nanotubes and others graphene-based nanostructures has become possible, draining a lot of research interests around them. Indeed graphene exhibits outstanding electronic, mechanical and thermal properties making it a great prospect for future in electronics and biophysics. It is in this context that hexagonal boron nitride (h-BN) has recently drawn a lot of attraction. It has been shown than one or a few single layer of h-BN may be folded to make nanotubes[2], which are very similar to semi-metallic carbon nanotubes, keeping however the insulating property of bulk hexagonal h-BN. In fact, the compatibility between graphene and hexagonal h-BN goes much deeper since both materials have the same structure, namely hexagonal 'honeycomb' lattice and, because of its insulating nature, hexagonal h-BN is often seen as the ideal substrate for conducting graphene[3].
That is why there has been a need of understanding the behavior of h-BN as well as the one of graphene. Mono-layer adsorption of h-BN on metals is important both from a theoretical and a technological point of view. For instance, it as been said that layered h-BN weakly interacts with a nickel substrate and remains stable up to high temperatures (1000K)[4]. This could provide a two dimensional insulator-metal interface well suited for nanostructured device fabrication.
In this thesis we not only focused on h-BN / Nickel interface but also on h-BN / Gold and h-BN / Iridium interfaces. These three materials present a inter atomic distance close enough to the lattice parameter of h-BN, thus a layer of BN can be easily adsorbed on each material in the (111) configuration. This reports sums up all the calculation and presents ours conclusions and future perspectives. It is organized as follows: in chapters 1 and 2, we will present all the theoretical and experimental backgrounds required to fully understand the exposed work. The study of the simple layer of h-BN will be depicted in chapter 3, then we will describe the interactions of this layer with a Nickel(111) slab in chapter 4. Finally, chapter 5 will present the study of h-BN over two other metals, gold and iridium, here the results are discussed.

Chapter 1

The Electronic problem

1.1 Basics

1.1.1 Schroedinger equation

To describe a many-body system, ie a system with A atoms and N electrons, one has to solve the well-known Schroedinger equation

$$H\Psi = [-\sum_{i}^{N} \frac{\hbar^2}{2m}\nabla_i^2 - \sum_{I}^{A} \frac{\hbar^2}{2m}\nabla_I^2 - \sum_{i,I} \frac{Z_i e^2}{\left|\vec{r_i} - \vec{R_I}\right|} + \sum_{i<j} \frac{e^2}{|\vec{r_i} - \vec{r_j}|} + \sum_{I<J} \frac{Z_I Z_J e^2}{\left|\vec{R_I} - \vec{R_J}\right|}]\Psi = E\Psi, \tag{1.1}$$

where i and I label namely electrons and atoms. The first two terms of the left part describe the kinetic energy of electrons and atoms whereas the three others are potentials for electron-atoms, electron-electron and atom-atom interactions. In order to simplify Eq. 1.1, the Born-Oppenheimer approximation allows to fix the position of the atoms. Thus their kinetic energy is canceled and the atom-atom interaction term becomes constant (E_{II} in Eq. 1.2)

$$H\Psi = [-\sum_{i}^{N} \frac{\hbar^2}{2m}\nabla_i^2 - \sum_{i,I} \frac{Z_i e^2}{\left|\vec{r_i} - \vec{R_I}\right|} + \sum_{i<j} \frac{e^2}{|\vec{r_i} - \vec{r_j}|} + E_{II}]\Psi = E\Psi. \tag{1.2}$$

In a cleaner version Eq. 1.2 can be written as

$$H\Psi = [T + V_{ext} + U]\Psi = E\Psi, \tag{1.3}$$

where T stands for the kinetic energy, U the electron-electron interaction potential and V_{ext}, the external potential, represents all the interactions with atoms. However, it is not possible to solve this equation as the wave functions Ψ depend on N variables in each space direction, ie $3N$ variables. Many methods have been developed to solve that many body equation and density functional theory is one of them.

1.1.2 Electronic Density

The probability to find an electron around the position $\vec{r}$ in a volume $d\vec{r}$ is

$$n(\vec{r})d\vec{r}, \tag{1.4}$$

where $n(r)$ is the electronic density of probability defined as

$$n(r) = N \int |\Psi(\vec{r_1}, \vec{r_2}...\vec{r_N})|^2 d^3_{r_1} d^3_{r_2} ... d^3_{r_N}. \tag{1.5}$$

This density owns two noteworthy properties:

$$\int n(\vec{r})d\vec{r} = N \tag{1.6}$$

$$n(\vec{r} \to \infty) = 0 \tag{1.7}$$

1.2 Mathematical Formalism

1.2.1 Hohenberg-Kohn Theorem

Besides the work made by Thomas and Fermi which led to the Thomas-Fermi model, the formulation of the Hohenberg-Kohn theorem in 1964 allowed the elaboration of the modern density functional theory. That theorem can be divided in two parts.

Theorem 1

> The external potential V_{ext} is univocally determined by the electronic density $n(\vec{r})$, besides a trivial additive constant.

The important conclusion of the first part of the theorem is its corollary

> Since $n(\vec{r})$ univocally determines V_{ext}, it also determines the ground state wave function Ψ, which should be obtained by solving the full many-body Schroedinger equation.

It means that if we know the electronic density of the ground state, all the properties of the system can be determined.

Theorem 2

> There is a functional of the density $E[n]$, good for any potential V_{ext}, expressing the energy as a function of the density. For each V_{ext}, the ground state energy is the value which minimizes this functional and the associated density is the exact ground state density $n_0(\vec{r})$

This functional is expressed as

$$E[n] = F[n] + \int V_{ext}(r)n(r)dr, \tag{1.8}$$

where $F[n]$ is a universal function including the kinetic energy and the electron-electron interaction potential, both depending on the electronic density.

$$F[n] = \langle \Psi | T[n] + U[n] | \Psi \rangle \tag{1.9}$$

1.2.2 Kohn-Sham equation

Even though it is with now possible to solve the many-body Schroedinger equation, one has however to know $F[n]$ which is –sadly– not possible. Indeed, it is not possible to give an analytical expression to the kinetic energy T in a system with N interacting electrons. Kohn and Sham's idea was to replace that system by another one of non-interacting electrons that produces the same electronic density. The main point is that in a such system the exact expression of the kinetic energy is known

$$T_s[n] = -\frac{\hbar^2}{2m} \sum_{i=1}^{N/2} \langle \phi_i | \nabla^2 | \phi_i \rangle. \tag{1.10}$$

Using Eq. 1.10, the universal function F can be re-written in:

$$F[n] = T_S[n] + \frac{1}{2} \int \int \frac{n(r)n(r')}{|r - r'|} dr dr' + E_{XC}[n], \tag{1.11}$$

the second term of Eq. 1.11 is nothing but the Hartree potential. E_{xc} stands for the exchange correlation potential which accounts for the kinetic effects ignored in T_s. With a quick substitution Eq. 1.8 becomes

$$E_{KS}[n] = T_S[n] + \frac{1}{2} \int \frac{n(r)n(r')}{|r - r'|} dr dr' + E_{XC}[n] + \int V_{ext}(r)n(r)dr. \tag{1.12}$$

By defining $V_s = V_{ext} + \frac{1}{2} \int \frac{n(r)n(r')}{|r-r'|} dr dr' + V_{xc}[n]$ where V_{xc} is the derivative of E_{XC}, one can then define the one-electron Kohn-Sham equations

$$[-\frac{\hbar^2}{2m} + V_s(\vec{r})]\phi_i(\vec{r}) = \epsilon_i \phi_i(\vec{r}), \tag{1.13}$$

which may be solved self-consistently. Basically the process is the following: starting from a empirical density, we compute the external potential V_s allowing us to get the Kohn Sham orbitals ϕ_i. Then we extract the density $n*(r) = \sum_i |\phi_i|^2$ that we inject at the beginning of the process until that the convergence of each value is reached.

1.2.3 Extension to spin-polarized systems

In order to extend Kohn-Sahm theory to spin-polarized systems it is sufficient to consider the electronic density as composed by two independent spin densities,

$$n(\vec{r}) = n(\vec{r}) \uparrow + n(\vec{r}) \downarrow \tag{1.14}$$

. Each of this densities is constructed with the Kohn-Sahm spin orbitals satisfying an equation similar to Eq. 1.13,

$$[-\frac{\hbar^2}{2m} + V_{SS}(\vec{r})]\phi_{i,s}(\vec{r}) = \epsilon_{i,s}\phi_{i,s}(\vec{r}), \tag{1.15}$$

where V_s becomes

$$V_{SS} = V_{ext} + \frac{1}{2}\int \frac{n(r)n(r')}{|r-r'|}drdr' + V_{xc}[n\uparrow, n\downarrow]. \tag{1.16}$$

Then the spin density are

$$n_s(\vec{r}) = \sum_i^{N/2} |\phi_{i,s}(\vec{r})|^2. \tag{1.17}$$

The spin-polarization density may be seen as

$$\zeta(\vec{r}) = n(\vec{r}) \uparrow - n(\vec{r}) \downarrow \tag{1.18}$$

The densities given in expressions 1.14 and 1.18 implies two different numbers $N\uparrow$ and $N\downarrow$ such as $N = N\uparrow + N\downarrow$. Note that it is not required to have $N\uparrow = N\downarrow$ and for instance in nickel $N\uparrow > N\downarrow$. The Kohn-Sahm energy functional is then

$$E_{KS}[n] = T_S[n\uparrow, n\downarrow] + \frac{1}{2}\int \frac{n(r)n(r')}{|r-r'|}drdr' + E_{XC}[n\uparrow, n\downarrow] + \int V_{ext}(r)n(r)dr, \tag{1.19}$$

with

$$T_s[n\uparrow, n\downarrow] = -\frac{\hbar^2}{2m}\sum_{s=1}^{2}\sum_{i=1}^{N/2}\langle\phi_{i,s}|\nabla^2|\phi_{i,s}\rangle. \tag{1.20}$$

Finally, there are systems where the projection of the total spin of the system is a not a good quantum number. The theory of this non-collinear magnetism is based on a 2×2 representation of the spin density

$$n_{\alpha\beta}(\vec{r}) = \frac{1}{2}n(\vec{r})\delta_{\alpha\beta} + \frac{1}{2}\sum_{i=1}^{3}\zeta_i(\vec{r})\sigma^i_{\alpha\beta}, \tag{1.21}$$

where σ^i are the Pauli spin matrices and ζ_i the Cartesian components of the spin polarization vector.

1.3 Approximation

Many approximations are currently implemented to approximate E_{xc}. In this thesis we mainly worked with the Generalized Gradient Approximation (GGA) with the Perdew-Burke-Ernzerhof functional (PBE)[5], that we will briefly describe here. It is worth noting that any approximation has the form

$$E_{XC}[n(r)] = \int n(\vec{r})\epsilon_{xc}(r)dr, \tag{1.22}$$

where $)\epsilon_{xc}$ is the exchange-correlation energy per particle.

1.3.1 Local Density approximation

Local Density approximation is the oldest and most famous approximation, proposed in the original Hohenberg and Kohn's paper[6]. Therefore, even if we didn't use it in our study, it has to be developed here. The main scope of LDA is to locally approximate the exchange correlation energy ϵ_{XC} of a system by the exchange correlation energy of a homogeneous free electron gas with the same density. The advantage is that the homogeneous free electron gas is the only system for which we can determine precisely the form of ϵ_{XC}. The functional of the total energy E_{XC} becomes

$$E_{XC}^{LDA}[n(r)] = \int n(\vec{r})\epsilon_{xc}^{hom}[n(r)]dr, \tag{1.23}$$

where $\epsilon_{xc}^{hom}[n(r)]$ is the exchange correlation functional of one particle in a homogeneous gas of density $n(r)$. Energy can be decomposed in two exchange and correlation contributions, namely E_X and E_C. E_X is the exchange energy functional defined by Dirac

$$E_X[n(r)] = -\frac{3}{4}(\frac{3}{\pi})^{1/3}\int n(r)^{4/3}dr. \tag{1.24}$$

While E_C derives from an interpolation formula between the known form of ϵ_C at high and low density limits.

1.3.2 Generalized Gradient approximation

In a way, the GGA is nothing but a enhancement of the local density approximation. The principle is to consider the spatial variation of the electronic density by accounting density gradient term $\nabla n(r)$. The total energy is seen as

$$E_{XC}^{GGA}[n(r)] = \int n(\vec{r})\epsilon_{xc}^{hom}[n(r)]F_{XC}[n(r), \nabla n(r)]dr, \tag{1.25}$$

with $F_{XC}[n(r), \nabla n(r)]$ being the enhancement factor.

Chapter 2

Surface states and Photo-emission Spectroscopy

As the one of the goal of this thesis is to compare DFT band structures with Angle Resolved Photo-emission Spectroscopy ones, it may be useful to briefly describe the ARPES principle.

2.1 Surface states

Surface states are the electronic states found at the edges of materials. They are aftermath of the brutal transition between the bulk material and the vacuum. It leads to a modification of the electronic band structure for atomic layers near the surface.

2.1.1 Surface states in metal

A simple model for representing surface states in metal is to consider a semi-infinite crystal in the one-dimensional nearly free electron model. In this model electron-ion and electron-electron interactions are neglected and the potential barrier which occurs at the surface (see Fig. 2.1) In a way only the lattice aspect and thus the periodic potential are emphasized. Schroedinger equation becomes

$$[-\frac{\hbar^2}{2m}\frac{d^2}{dz^2} + V(z)]\Psi(z) = E\Psi(z), \tag{2.1}$$

Bulk states

The potential in the crystal V is periodic with a periodicity of a, the lattice parameter. And it is constant equal to V_0 in the vacuum region.

$$V(z) = \begin{cases} V(z+la) & \texttt{for} \quad z < 0 \\ V_0 & \texttt{for} \quad z > 0 \end{cases}, \tag{2.2}$$

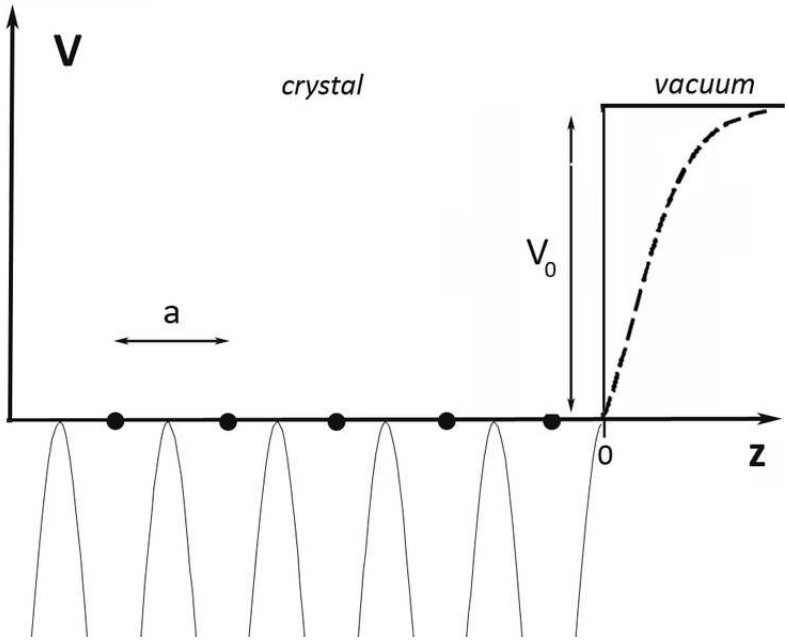

Figure 2.1: Simple one dimensional model of a periodic potential terminating at an ideal surface. Dashed line represents a more realistic model, where the potential barrier is more smooth.

where l is an integer. This is nor more than the well known problem of the potential barrier (or quantum well) for a nearly free electron gas. One can splits the problem in two parts and use the continuity of the wave function and its derivative at $z = 0$. Since the potential is periodic in the bulk the solutions are Block functions, more precisely the sum of an incident wave and a reflected one. In the vacuum, i.e. when $z > 0$, the solution is a decreasing exponential:

$$\Psi(z) = \begin{cases} Au_k \exp^{-ikz} + Bu_k \exp^{ikz}, & \texttt{for} \quad z < 0 \\ C \exp^{-\sqrt{\frac{2m(V_0-E)}{\hbar^2}}z}, & \texttt{for} \quad z > 0 \end{cases} \tag{2.3}$$

That solution is qualitatively exposed in the top part of Fig. 2.3. To sum up it is important to note that for the bulk states, wave functions oscillate deep into the crystal and decay quickly in the vacuum.

Surface states

If we look now at wave vectors near the boundary of the Brillouin Zone (or Bragg plane) $G = 2\pi/a$, we can write the solution as a linear combination of plane waves with wave vectors k and $k - G$:

$$\Psi_k(z) = \alpha \exp^{ikz} + \beta \exp^{i(k-G)z}. \tag{2.4}$$

In that region, the potential can be seen as

$$V(z) = -V_0 + 2V_g \cos(Gz). \tag{2.5}$$

Again we split the problem in two parts according to whether we are in the crystal or not:

$$\Psi(z) = \begin{cases} A_k \exp^{-sz}, & \texttt{for} \quad z > 0 \\ \exp^{qz+ikz}(C_k + C_{k-G} \exp^{-iGz}). & \texttt{for} \quad z < 0 \end{cases} \tag{2.6}$$

For an infinite crystal, in order to satisfy the Born-von Karman (BVK) boundary conditions, it is required for k to be real. Here, near the surface the BVK conditions are not satisfied and k can be imaginary. It yields then a decaying wave into the crystal as showed in the bottom part of Fig. 2.3. Note that the wave function inside the crystal has to match the function outside. It provides continuity conditions for Ψ and its derivative at $z = 0$ and allows to find the parameters s and q. The eigenvalues E are the solutions of the secular equation

$$\begin{pmatrix} k^2 - V_0 - E & V_g \\ V_g & (k-g)^2 - V_0 - E \end{pmatrix} \begin{pmatrix} \alpha \\ \beta \end{pmatrix} = 0, \tag{2.7}$$

The function $E(k^2)$ is plotted in Fig. 2.2. For bulk states, a gap appears at $k = \frac{nG}{2}$ with n

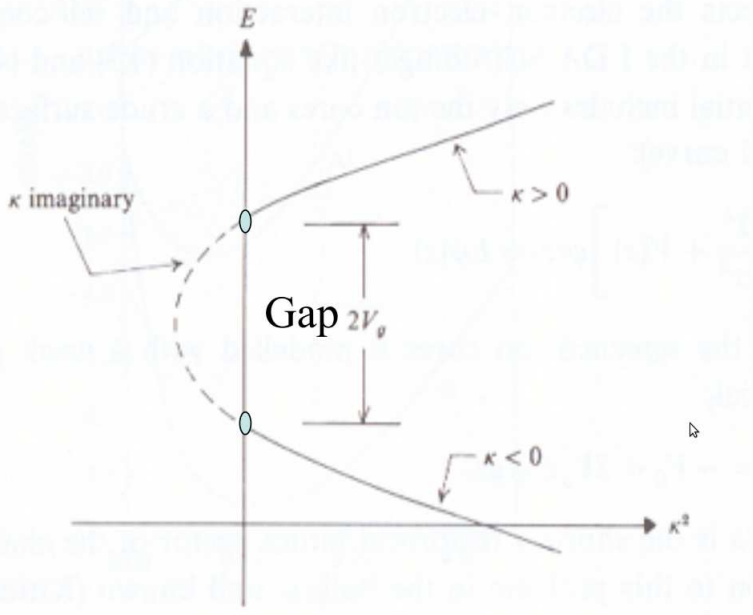

Figure 2.2: $E(\kappa^2)$ for the one-dimensional semi-infinite nearly-free electron model

an integer. Since the imaginary values of k are allowed for the surface states, it means that extra states in the gap exist at the surface of a material. However it is worth to note that the matching conditions at the surface implies a negative value of the periodic potential V_g.

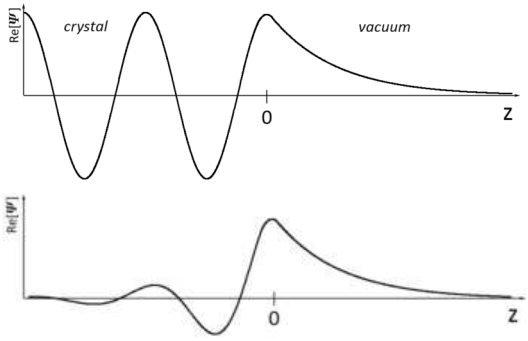

Figure 2.3: (top) Real part of solution to the one-dimensional Schrödinger equation, which correspond to the bulk states. (bottom) Real part of the solution to the one-dimensional Schrödinger equation, which correspond to surface states.(source:Wikipedia)

2.2 Angle Resolved Photo emission Spectroscopy

ARPES can directly map the band structure of solid materials. This advantage, added to its applicability to numerous systems has made ARPES a widely used technique to study solid state materials.

2.2.1 Technical Principle

The main origin of photoelectrons spectroscopy stands in the famous photoelectric effect first observed by Hertz, the explained by Einstein. Basically, when light (and then photons) is incident on a sample, an electron of the sample can absorb the energy of a photon and escape from the material. The minimum energy of the incident photon $h\nu$ has to be equal to W the work function of the material, ie the required energy to free an electron from the material. In the general case the kinetic energy of the newly freed electron E_{kin} is

$$E_{kin} = h\nu - W - E_B, \tag{2.8}$$

where E_B is the binding energy of the electron. Then by looking at E_{kin}, the energy of an electron inside the material can be known;form the same photon energy, core electrons will have a lower E_{kin} than valence electrons. Once E_{kin} is determined, it is possible to fetch the wave vector or momentum $\vec{k} = \frac{\vec{p}}{\hbar}$ of the photoelectrons. Its modulus is $|k| = \frac{\sqrt{2mE_{kin}}}{\hbar}$ and its component parallel $\vec{k}_{\|}$ and perpendicular $\vec{k}_{\perp}$ are given in term of the polar θ and azimuthal ϕ angles defined by the experiment [7]. However, since the electrons are being projected through the surface, the momentum perpendicular to the surface is not conserved. Therefore, angle-resolved photo emission is ideal for 2D materials where the principle momentum directions of interest are parallel to the surface. In practice, the electrons ejected from the material are collected using a hemispherical detector where both the kinetic energy and the emission

angle of the electrons are recorded. The sample and the detector are kept in an ultra high vacuum (UHV) chamber in order to minimize surface contamination. Light sources are either synchrotron radiation at 20-100eV, plasma Helium discharge at 20eV, or more recently, modern-day lasers 6 eV. Figure 2.4, depicts a general overview of the experimental system.

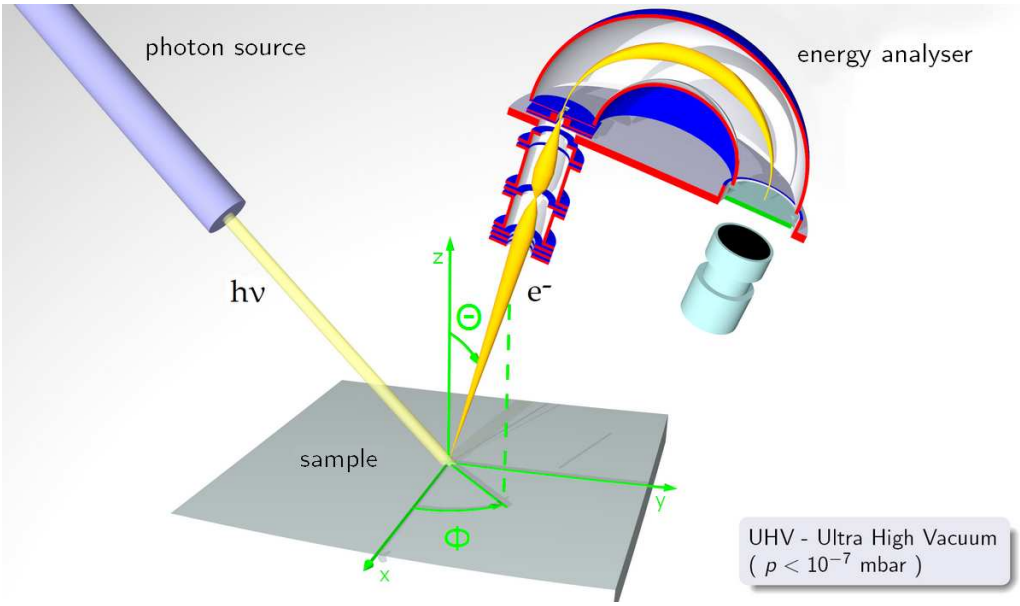

Figure 2.4: An experimental set up of ARPES. (source Wikipedia)

2.2.2 Theoretical Description

To develop a coherent description of the photo emission process, one has to calculate the transition probability p_{fi} between the ground states Ψ_i^N and one possible final state Ψ_f^N, N being the number of electrons in the ground state. This can be done thanks to the Fermi's golden rule:

$$p_{fi} = \frac{2\pi}{\hbar}|\langle\Psi_f^N|H_{int}|\Psi_i^N\rangle|^2\delta, \tag{2.9}$$

where δ is the final density of states and is a function of E_i^N, E_f^N the initial and final energies of the N particle system. The interaction with the photons is given by the Hamiltonian:

$$\begin{aligned} H_{int} &= \frac{e}{2mc}(\mathbf{Ap} + \mathbf{pA}) \\ &= \frac{e}{mc}\mathbf{Ap}, \end{aligned} \tag{2.10}$$

where $\mathbf{p}$ is the electronic momentum operator and $\mathbf{A}$ is the electromagnetic vector potential.$\mathbf{Ap}$ is called the direct transmission term and is the dominant contribution to the photo emission intensity.

Chapter 3

Structural and Electronic properties of Hexagonal - Boron Nitride

3.1 Definition

3.1.1 Overview

Hexagonal - Boron Nitride (h-BN) is a crystal composed in the same amount of boron and nitrogen atoms. It may occur under different forms (cubic, wurtzite, hexagonal), and is well famous for outstanding properties as high thermal conductivity, elasticity, chemical stability[8] When in hexagonal form, boron nitride exhibits the same structure than graphite, adopting a layered structure. Thus, as for graphite, it is possible to extract one or a few layers of boron nitride. The latter has the same honeycomb structure than graphene but a slightly larger lattice constant (1.8% larger). But when graphene is reported to be semi-metallic with a zero-gap at the Dirac point, h-BN owns insulator properties. Indeed, the strong difference in electronegativity between boron and nitrogen atoms leads to the opening of a wide gap of about 5.9eV.

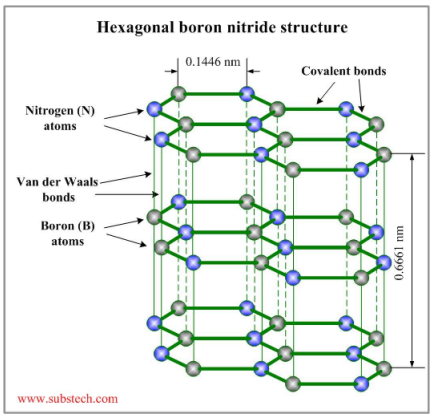

Figure 3.1: Stacking of hexagonal boron nitride

As figure 3.1 shows, h-BN has a peculiar stacking. The stacking is alternated since a nitride atom is always stacked over a boron atom and vice versa. That stacking yields B-N interlayer binding, harder to break than the C-C (carbon-carbon) binding and that is why it is more difficult to synthesize h-BN than graphene.

3.1.2 Bonding

Since boron and nitrogen are both direct neighbors to carbon in the periodic table, BN displays same electronic configuration than carbon. The electronic structure of graphite is $1s^2 2s^2 2s^2$. Electrons on the deepest layer are core electrons, strongly bound to the atom and do not participate to the transport phenomena. Which left us with 4 valence electrons located on orbitals $2_s, 2p_x, 2p_y$ and $2p_z$. In hexagonal lattice, the s, p_x, p_y orbitals hybridize to yield the sp^2 orbital. Each carbon atom owns three in plane sp^2 orbitals making a $\frac{2\pi}{3}$ angle between them. The overlap between two sp^2 orbitals creates the sp^2–sp^2 bond or σ bond, the strongest covalent bonding. The p-orbital remaining $(2p_z)$ forms the out of the plane π bond. That orbital is delocalized and responsible for the conduction effects, and we will then mainly focus on this one.

3.2 Crystallography

3.2.1 Structural parameters

Hexagonal boron nitride is composed of boron and nitrogen atoms disposed in a honeycomb lattice. A honeycomb lattice can be seen as the superposition of two triangular lattices A and B. We define the basis of primitive vectors $E = (a_1, a_2)$:

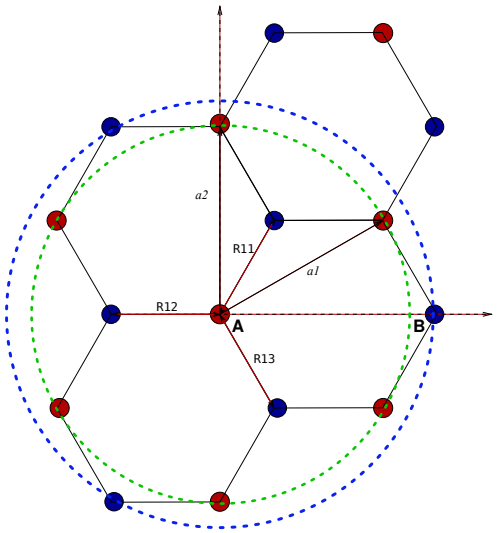

Figure 3.2: Hexagonal lattice of h-BN constructed by two superposed triangular sub-lattices, A and B. Red circle denotes the second nearest neighbors of the centered atom, blue circle the third nearest.

$$a_1 = a \begin{pmatrix} \frac{\sqrt{3}}{2} \\ \frac{1}{2} \\ 0 \end{pmatrix} \quad a_2 = a \begin{pmatrix} 0 \\ 1 \\ 0 \end{pmatrix} \tag{3.1}$$

Where $a = 2.5$ Å is the lattice constant. Note that there is a 1.8% mismatch with respect to the lattice parameter of graphene. For 3D crystals we can also add the a_3 vector in the basis:

$$a_3 = c \begin{pmatrix} 0 \\ 0 \\ 1 \end{pmatrix} \tag{3.2}$$

Where $c = 6.61$ Å is the distance between two identical layers.

3.2.2 Reciprocal space

We can extract the reciprocal space which will be useful for calculations and analysis. The reciprocal basis $B = (b_1, b_2, b_3)$ is generated using the formula:

$$\vec{b_k} = \frac{2\pi . \vec{a_i} \times \vec{a_j}}{V} \tag{3.3}$$

Where i, j, k are circular permutations, V the mix product between the three vectors, i.e. the volume of the unitary cell. Then we get the 2D reciprocal vectors:

$$b_1 = k_D \begin{pmatrix} 1 \\ 0 \\ 0 \end{pmatrix} b_2 = k_D \begin{pmatrix} \frac{-1}{2} \\ \frac{\sqrt{3}}{2} \\ 0 \end{pmatrix} \tag{3.4}$$

And with $k_D = \frac{4\pi}{\sqrt{3}a}$. The corresponding Brillouin zone is depicted in Fig. 3.3, together with the two high-symmetry points K and M.

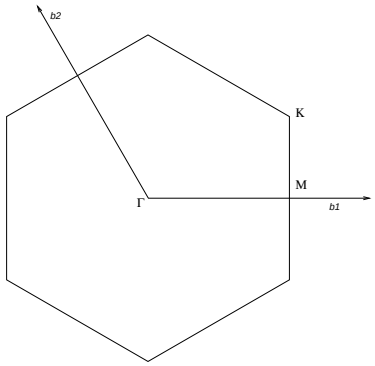

Figure 3.3: Brillouin zone of hexagonal BN. M and K are the two high-symmetry points $M = \frac{4\pi}{a\sqrt{3}}(\frac{1}{2}, 0)$ and $K = \frac{4\pi}{a\sqrt{3}}(\frac{1}{2}, \frac{1}{2\sqrt{3}})$ in cartesian coordinates.

3.3 Tight Binding Model for boron nitride

3.3.1 General approach

In our study we model the π and π^* band energy dispersion using a simple nearest-neighbor as well as third nearest-neighbor tight-binding (3NN TB) parametrizations. We followed the method described in references [9] and [10]. Let $\phi_\alpha(\mathbf{r} - \mathbf{R}_\alpha)$ be the orbital function of an electron at the cell $\mathbf{R}$ of the sub-lattice α (see Fig. 3.2). We construct then the tight binding function satisfying the Bloch theorem:

$$\Phi_\alpha(\mathbf{r}, \mathbf{k}) = \frac{1}{\sqrt{N}} \sum_{\mathbf{R}} e^{i\mathbf{k}.\mathbf{R}} \phi_\alpha(\mathbf{r} - \mathbf{R}_\alpha),\ \alpha = A\ or\ B, \tag{3.5}$$

where N stands for the number of unit cells. Using the matrix representation in the Φ basis, the problem comes to solving the secular equation of the following matrix:

$$M = \begin{pmatrix} H_{AA}(\mathbf{k}) - E(\mathbf{k})S_{AA}(\mathbf{k}) & H_{AB}(\mathbf{k}) - E(\mathbf{k})S_{AB}(\mathbf{k}) \\ H_{AA}(\mathbf{k})^* - E(\mathbf{k})S_{AA}(\mathbf{k})^* & H_{BB}(\mathbf{k}) - E(\mathbf{k})S_{BB}(\mathbf{k}). \end{pmatrix} \tag{3.6}$$

where

$$H_{ij} = \langle \phi_i(\mathbf{r} - \mathbf{R}_i)|H|\phi_j(\mathbf{r} - \mathbf{R}_j)\rangle \tag{3.7}$$
$$S_{ij} = \langle \phi_i(\mathbf{r} - \mathbf{R}_i)|\phi_j(\mathbf{r} - \mathbf{R}_j)\rangle \tag{3.8}$$

In our calculations we neglected the overlap S between the orbitals (we supposed that they are totally orthogonal) and then the resolution of $det(M) = 0$ yields the eigenenergies E($\mathbf{k}$).

3.3.2 A minimal Tight-Binding model for boron nitride

Nearest Neighbor Model

Let's evaluate the elements described in Eq. (3.8) in the case of hexagonal boron nitride. In case of interactions between equivalent atoms (belonging to the same sub lattice and therefore on the matrix diagonal) we have

$$\begin{aligned} H_{AA} &= \frac{1}{N}\sum_{\mathbf{R}_A}\sum_{\mathbf{R}_{A'}} e^{i\mathbf{k}(\mathbf{R}_{A'}-\mathbf{R}_A)}\langle \phi_A(\mathbf{r} - \mathbf{R_A})|H|\phi_A(\mathbf{r} - \mathbf{R}_{A'})\rangle \\ &= \frac{1}{N}\sum_{\mathbf{R_A}} \langle \phi_A(\mathbf{r} - \mathbf{R}_A)|H|\phi_A(\mathbf{r} - \mathbf{R}_A)\rangle = \epsilon_{p_z}, \end{aligned} \tag{3.9}$$

where N is the number of unit cells, $\mathbf{R}_A$ and $\mathbf{R}_{A'}$ are the position of atoms A and A'. According to the denomination used in [10], ϵ_{p_z} describes the energies of electrons on the $2p_z$ orbital. When it came to interaction between electrons bound to nonequivalent atoms we considered in a first time the nearest neighbor approximation. In a honeycomb lattice it means than an atom will interact only with its three nearest neighbors (see Fig. 3.2)

$$H_{AB} = \frac{1}{N}\sum_{\mathbf{R}_A}\sum_{\mathbf{R}_B} e^{i\mathbf{k}(\mathbf{R}_B-\mathbf{R}_A)}\langle \phi_A(\mathbf{r} - \mathbf{R_A})|H|\phi_B(\mathbf{r} - \mathbf{R}_B)\rangle. \tag{3.10}$$

Using the fact that there is translational invariance in a Bravais lattice, the sum over each atom of a sub lattice is done N times and therefore Eq. (3.10) becomes

$$H_{AB} = \sum_{\mathbf{R}_A} e^{i\mathbf{k}(\mathbf{R}_B-\mathbf{R}_A)}\langle \phi_A(\mathbf{r} - \mathbf{R_A})|H|\phi_B(\mathbf{r} - \mathbf{R}_B)\rangle \quad = \gamma_0(e^{i\mathbf{k}\mathbf{R}_{11}} + e^{i\mathbf{k}\mathbf{R}_{12}} + e^{i\mathbf{k}\mathbf{R}_{13}}) \tag{3.11}$$

with the hopping parameter equal to

$$\gamma_0 = \langle \phi_A(\mathbf{r} - \mathbf{R_A})|H|\phi_B(\mathbf{r} - \mathbf{R}_A - \mathbf{R}_{1i})\rangle \quad (i = 1, 2, 3), \tag{3.12}$$

and $\mathbf{R}_{1i}$ the distance between an atom and its three nearest neighbors

$$\mathbf{R}_{11} = \frac{1}{3}(\mathbf{a}_1 + \mathbf{a}_2) = \frac{a}{3}\begin{pmatrix} \frac{\sqrt{3}}{2} \\ \frac{3}{2} \end{pmatrix} \tag{3.13}$$

$$\mathbf{R}_{12} = \frac{a}{3}\begin{pmatrix} \cos\frac{2\pi}{3} & \sin\frac{2\pi}{3} \\ -\sin\frac{2\pi}{3} & \cos\frac{2\pi}{3} \end{pmatrix} \cdot \begin{pmatrix} \frac{\sqrt{3}}{2} \\ \frac{3}{2} \end{pmatrix} = \frac{a}{6}\begin{pmatrix} \sqrt{3} \\ -3 \end{pmatrix} \tag{3.14}$$

$$\mathbf{R}_{13} = \frac{a}{6}\begin{pmatrix} \cos\frac{2\pi}{3} & \sin\frac{2\pi}{3} \\ -\sin\frac{2\pi}{3} & \cos\frac{2\pi}{3} \end{pmatrix} \cdot \begin{pmatrix} \sqrt{3} \\ -3 \end{pmatrix} = \frac{a}{6}\begin{pmatrix} -2\sqrt{3} \\ 0 \end{pmatrix} \tag{3.15}$$

We also define the function

$$f(\mathbf{k}) = e^{i\mathbf{k}\mathbf{R}_{11}} + e^{i\mathbf{k}\mathbf{R}_{12}} + e^{i\mathbf{k}\mathbf{R}_{13}} \tag{3.16}$$

$$= e^{-\frac{iak_x}{\sqrt{3}}} + 2e^{\frac{iak_x}{2\sqrt{3}}}\cos(\frac{a}{2}k_y). \tag{3.17}$$

With all that parameters we get the matrix (also depicted in reference [11])

$$H = \begin{pmatrix} \epsilon_b & \gamma_0 f(\mathbf{k}) \\ \gamma_0 f(\mathbf{k})^* & \epsilon_n \end{pmatrix}, \tag{3.18}$$

Where ϵ_b and ϵ_n are the on site energies, namely at boron and nitrogen sites. According to [11], the eigenvalues of Hamiltonian H (Eq. (3.18)), are given by

$$E = E_0 \pm \frac{1}{2}\sqrt{E_g^2 + 4|f|^2}, \tag{3.19}$$

where $E_0 = \frac{\epsilon_b + \epsilon_n}{2}$ and $E_g = \epsilon_b - \epsilon_n$ is the energy gap.

Third Nearest Neighbors Model

With the third nearest neighbor model, we not only consider the nearest atom but also the second nearest and the third nearest (see Fig.3.2).The Hamiltonian for a mono-layer of $h - BN$ crystal is then modified [12] and Eq. (3.18) becomes

$$H = \begin{pmatrix} \epsilon_b + \gamma_1 g(\mathbf{k}) & \gamma_0 f(\mathbf{k}) + \gamma_2 h(\mathbf{k}) \\ \gamma_0 f(\mathbf{k})^* + \gamma_2 h(\mathbf{k})^* & \epsilon_n + \gamma_1 g(\mathbf{k})^* \end{pmatrix}, \tag{3.20}$$

where $\gamma_0, \gamma_1, \gamma_2$ are the hopping parameters, while $g(\mathbf{k})$ and $h(\mathbf{k})$ are functions relative to the namely second and third nearest neighbors respectively:

$$g(\mathbf{k}) = \sum_{i=1}^{6} \exp^{i\mathbf{k}\mathbf{R}_{2i}} \tag{3.21}$$

$$= 2\cos(ak_y) + 2\cos(k_x a\frac{\sqrt{3}}{2} + k_y\frac{a}{2}) + 2\cos(k_x a\frac{\sqrt{3}}{2} - k_y\frac{a}{2}), \tag{3.22}$$

and

$$h(\mathbf{k}) = \sum_{i=1}^{3} \exp^{i\mathbf{k}\mathbf{R}_{3i}} \tag{3.23}$$

$$= \exp^{i\frac{2a}{\sqrt{3}}k_x} + \exp^{-ia\frac{k_x}{\sqrt{3}}} 2\cos(ak_y). \tag{3.24}$$

In section 3.4 we used the DFT theory to fit the unknown parameters, i.e γ_i and E_g.

3.4 Density Functional Theory

3.4.1 Methodology

The most of the theoretical calculations have been carried out using the DFT, *ab-initio*, theory as implemented in *GPAW* code [13], from the DTU. Unlike more famous DFT-codes, *GPAW* uses real-space uniform grids and multi-grid methods or atom-centered basis-functions.

3.4.2 Band Structure

Before going further with transition metals, it may be useful to have a look at the h-BN band structure. Fig. 3.4 shows the band structure of hexagonal BN. We used a 17x17x1 Monkhorst-Pack grid to calculate the electronic density and GGA-PBE pseudo-potentials. The k-path is divided in two directions, from $M = (\frac{1}{2}, 0, 0)$ to $\Gamma = (0, 0, 0)$ and from Γ to $K = (\frac{2}{3}, \frac{1}{3}, 0)$. Each part of the path includes the same number of points, namely 40. The gap is located at the K point and its value is around 4.7eV, which is in fairly good agreement with GGA calculations. As it is known than DFT calculation underestimates the gap, a GW-correction should be applied to find the commonly agreed value of 5.9eV.

3.4.3 Tight Binding fit to the DFT

We combined the tight binding model with a least-square method in order to find the best values for the parameters and to fit the π-band to the DFT one. The two π-bands are overlaid in Fig. 3.5 and the tight binding parameters are reported in Table 3.1. Despite a little offset the fit is rather good and the values reported in Table 3.1 are in good agreement with other works [11, 14]. The resulting band gap E_g stands in the range of the values reported in literature. Now that the reliability of our tight-binding model has been shown, we may apply it to other systems, i.e. h-BN on Ni(111) (see chapter 4).

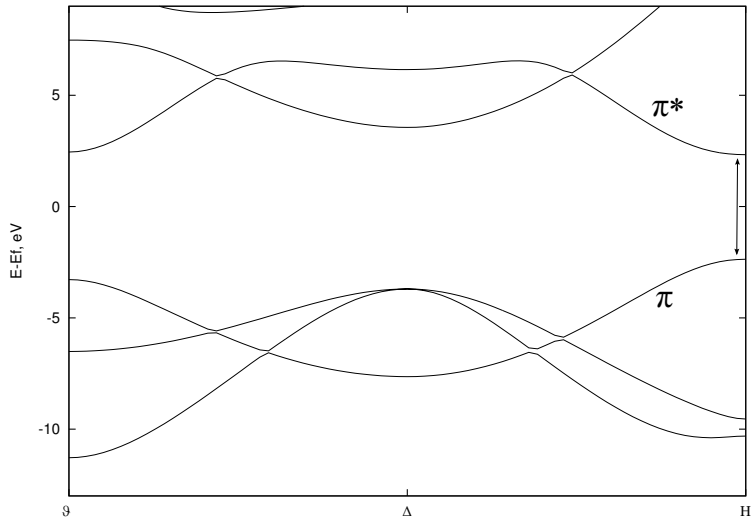

Figure 3.4: Band structure of one layer of hexagonal BN

γ_0	γ_1	γ_2	ϵ_n	ϵ_b	E_g
-2.16	-0.04	-0.08	-2.55	2.46	5.01

Table 3.1: Tight binding parameters calculated from the best fit to DFT data

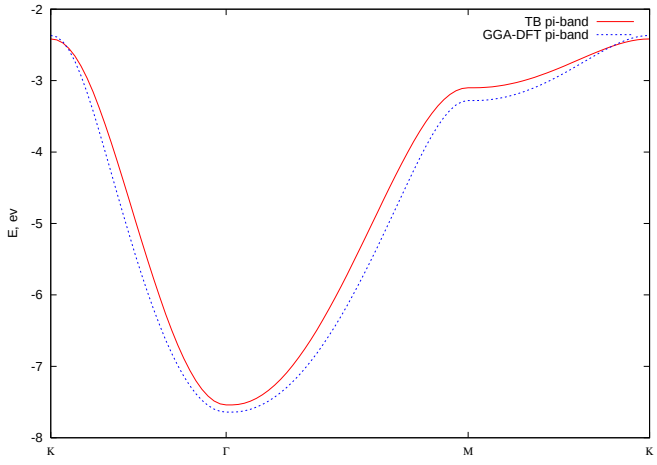

Figure 3.5: Comparison between the DFT π-band (blue) and the tight binding one (red). The K-path is the same as in reference [11], ie $K\Gamma MK$.

Chapter 4

Electronic properties of h-BN / $Ni(111)$ interface

4.1 Geometric Structure

4.1.1 $Ni(111)$ surface

Nickel is a ferromagnetic metal from the tenth column of the periodic classification. For that it is also called a transition metal. Its crystallographic structure is cubic-face-centered (FCC). In the (111) direction, FCC materials exhibit a three level stacking ABC, as Fig. 4.1 shows.

4.1.2 (1x1) h-BN on $Ni(111)$

h-BN, grows epitaxially on Ni(111) as experiments [15, 16] refer. The positions of boron and and nitrogen atoms with respect to the Ni(111)-surface sites are known from several experiments: *top*, *fcc* and *hcp*. We label these six possible configurations by their N and B positions. In close-packed layer system the fcc sites is occupied in every third layer (ABCABC ...), while the *hcp* site is occupied in every second layer (ABAB ...), while in the *top* configuration, either B or N atom is on top of the top-most Ni atoms.

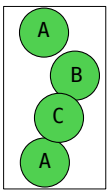

Figure 4.1: 7 layers stacking of $Ni(111)$

Grad et *al* [4], have performed total energy calculation for the six different configuration (see Fig. 4.2). They found out that two states are energetically favorable, each one with nitrogen atoms on top of the first layer and boron atom either on *hcp* or *fcc* sites. Huda and *al* tried to determine which one was the most likely to occur, but they couldn't due to the precision of GGA-LDA calculation. However they both agreed on the distance between h-BN and $Ni(111)$, namely 2.19 Å.

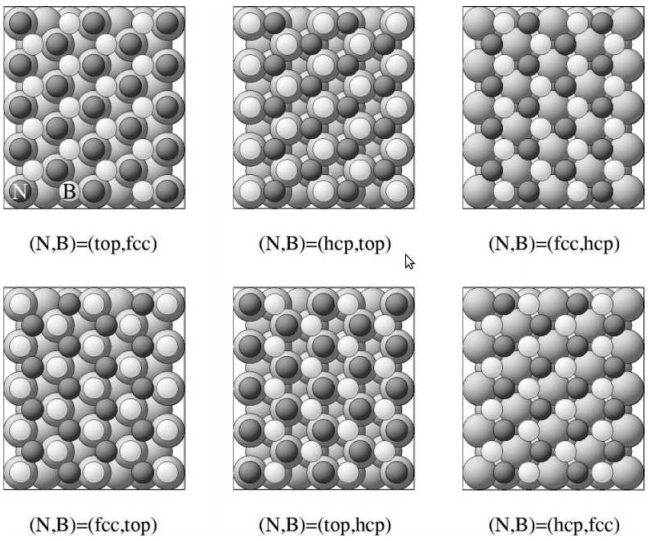

Figure 4.2: Six possible configurations for h-BN on top of $Ni(111)$

4.1.3 Structural properties of the h-BN / $Ni(111)$ interface: Corrugation

The lattice parameter of h-BN, is 2.5 Å and the distance between two Ni atoms is about 2.489 Å. The two distances are very close and that is why Ni is one of the best metal to be considered for interactions with both h-BN and graphene, whereas the structure still exhibits a mismatch of 0.4%. In literature it is widely discussed [15] that h-BN tends to compress its lattice yielding a corrugation effect of about 0.1 Å in order to compensate this mismatch. Unlike [4] and [17], we chose to consider this corrugation effect in our calculations (see Sec. 4.2.1).

4.2 Electronic properties of the h-BN / $Ni(111)$ interface

After convergence studies made with GPAW, we chose the following configuration. A 13 layers thick slab of Nickel has been sandwiched by two layers of corrugated h-BN. This

kind of configuration is in order to avoid the dipolar moment which would occur due to an asymmetric adsorption [17]. The basic super-cell contains 17 atoms, namely 13 Nickel, 2 Boron and 2 Nitrogen. If not told, all the calculations have been carried out using the Perdew-Burke-Ernzerhof exchange correlation functional implemented in GPAW. We used a spatial grid of 0.13 Å along the x, y directions and 0.16 Å along the z-axis. A $17 \times 17 \times 1$ sampling of the Brillouin zone has been used. We used periodic boundary conditions with a 15 Å vacuum length between each slabs.

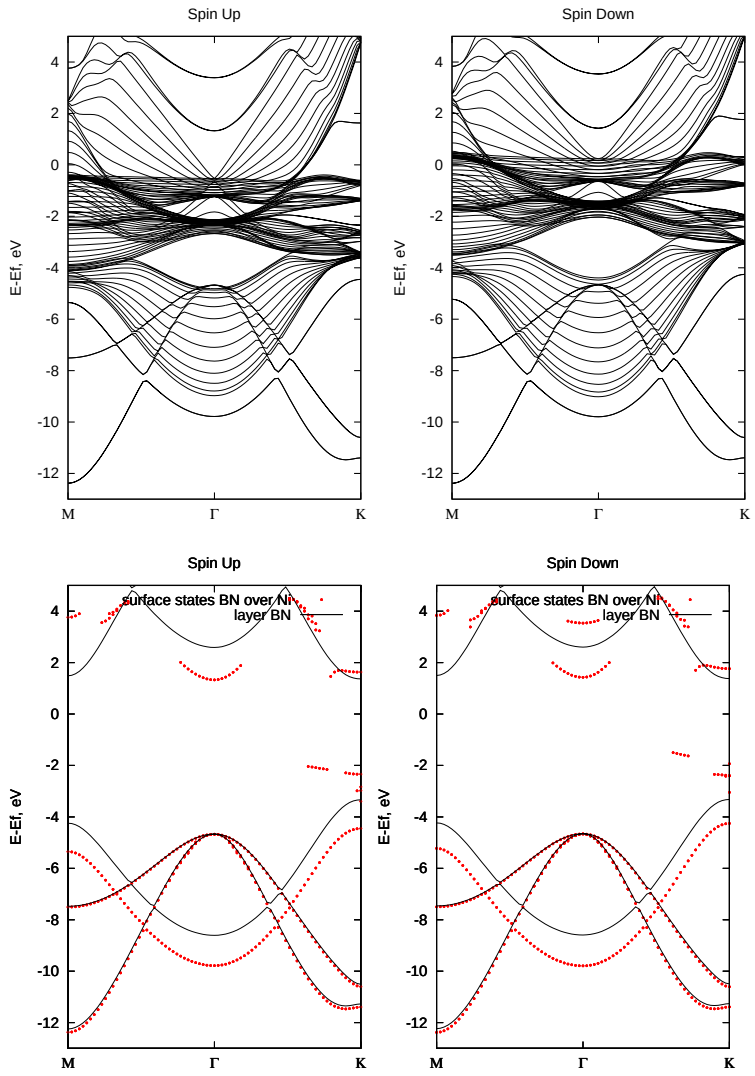

Figure 4.3: top: band structure of h-BN over $Ni(111)$ in spin up (left) and spin down (right) configuration. Bottom: Only the surface states (red) are represented as well as the band structure of bare h-BN (black).

Figure 4.3 presents the theoretical band structure of h-BN on a $Ni(111)$ slab. For the comparison we also added the ban. In order to see the influence of the $Ni(111)$ slab substrate, we extracted the surface states that we can suppose being mostly induced by the h-BN layer and we compare them with the original h-BN band structure (see Sec. 3.4.2). At a first glance, h-BN seems to keep the same band structure whether it is on top on nickel or not. But we also see that, when on top on nickel, the π-band is lowered with a shift down of about $1.2\,eV$. In other words, the π-band moves away from the Fermi level. As we stated in Chap. 3 that the π-band was responsible of conduction effect, we deduced than the insulating nature of h-BN remains and is even enhanced. However, the fact that STM measurements may be performed on h-BN/$Ni(111)$ [16] does indicate a metalicity of the slab, since electrons are able to tunnel trough the h-BN layer.

The comparison between the surface states obtained at DFT level with the ARPES experimental data are reported Fig. 4.4. It is obvious that the theoretical π-band follows reasonably well the experimental one, that is why we can affirm that our calculations are in good agreement with ARPES experiments. However there is still a small shift between the two bands at the Gamma point and Sec. 4.2.1 shows that taking into account the corrugation of h-BN reduces this shift.

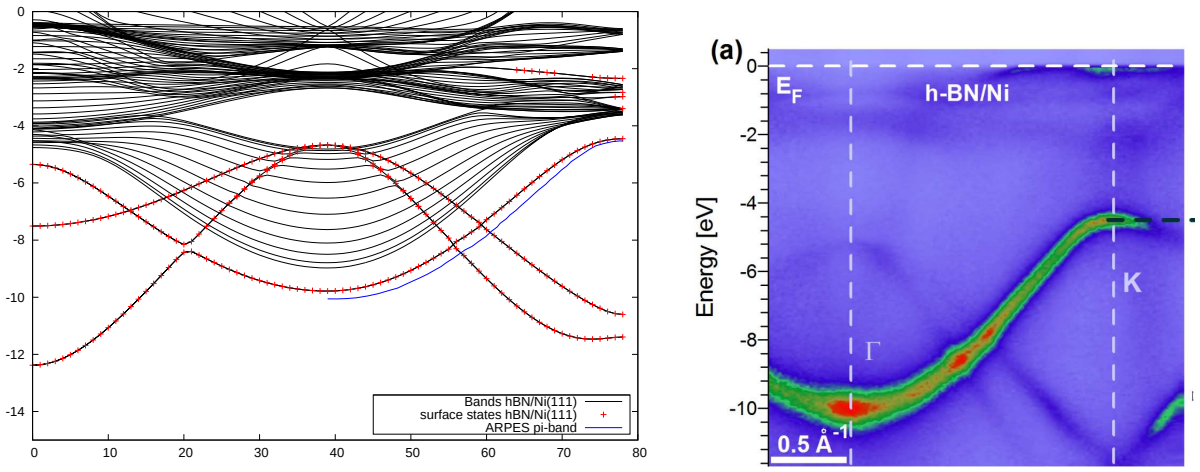

Figure 4.4: left: Comparison between ARPES experimental data (blue line) and theoretical (red dashed line) surface states. Black curves represent the whole theoretical band structure (with inner states). right: ARPES band structure of h-BN/Ni

4.2.1 Corrugation of h-BN

Unlike previous studies ([17, 4]), we also considered corrugated h-BN on top of $Ni(111)$. Indeed, as the lattice parameter of h-BN (2.5 Å) and the atomic distance between two Ni atoms (2.489 Å) are very close, one can suppose that h-BN compressing the h-BN lattice

parameter to 2.489 Åwill not considerably impact the band structure. It implies, as reported is Sec. 4.1.3, that h-BN stands buckled over the Ni layer.

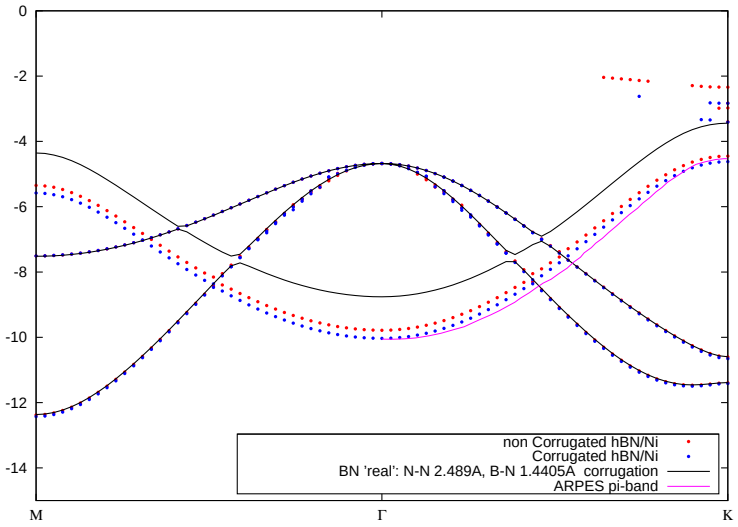

Figure 4.5: Comparison between flat (red line) and buckled (blue) h-BN over Ni. Pristine, corrugated h-BN (black line) is shown in order to see that the substrate effect remains.

Figure 4.5 depicts the effect on the π-band, when this buckling is taken into account. It clearly shows that the corrugation tends to shift down the π-band, and thus the fit with the experimental π-band is better. Finally, even if the corrugation effect does not change substantially the band structure, it still allows DFT calculation to be in better agreement with experiment.

4.2.2 Spin polarization

It is remarkable that the energies of the h-BN induced π-band seem to depend on the spin of the electrons. A closer look at the surface states of the band structure depicted in plot 4.3 allows us to see the effect on this polarization. As it is shown in Fig. 4.6, the π-band at M and K high symmetry point changes as a function of the spin polarization.

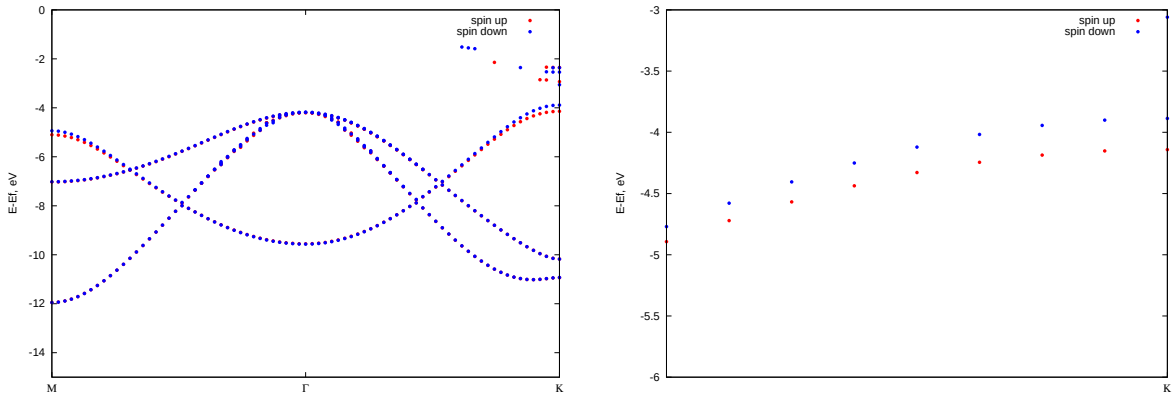

Figure 4.6: (left) Superposition of spin up (blue dashed line) and spin down (red dashed line) pi-bands for BN over $Ni(111)$. (right) Zoom of the same plot at point K

One can infers that it may implies magnetism for h-BN, but it does not since none of this band crosses the Fermi level. However, the magnetism of Ni is reflected in the fact that the $Ni(111)$ d-bands are partially empty (above the Fermi level) in the spin-down configuration. ARPES experiment does not report any spin polarization effect so one can wonder whether this effect is induced by the DFT analysis or the polarization of h-BN is real over a $Ni(111)$ substrate. We thought that a different approximation, namely the tight binding one, may bring us more informations.

4.3 Tight binding approximation

4.3.1 Hamiltonian

In order to have a better look at the behavior of the π-band we also use the tight binding approximation. We got inspired from the tight binding description of bilayer graphene. We considered one unit cell of h-BN over commensurate $Ni(111)$ such as the nitrogen atom stands over the nickel atom and the boron atom stands over vacuum. With that it is possible to define the 4×4 Hamiltonian following the same method than in reference [12].

$$H = \begin{pmatrix} E_n + h_0 f_2(\mathbf{k}) & g_0 f_1(\mathbf{k}) + m_0 f_3(\mathbf{k}) & t & 0 \\ g_0 f_1(\mathbf{k})^* m_0 f_3(\mathbf{k})^* & E_b + h_0 f_2(\mathbf{k})^* & 0 & 0 \\ t & 0 & E_{ni} + h_1 f_2(\mathbf{k}) & g_1 f_1(\mathbf{k}) + m_1 f_3(\mathbf{k}) \\ 0 & 0 & g_1 f_1(\mathbf{k})^* + m_1 f_3(\mathbf{k})^* & 0 + h_1 f_2(\mathbf{k})^* \end{pmatrix}, \tag{4.1}$$

where E_n, E_b, E_{ni} represent namely the on-site energies of nitrogen, boron, and nickel. g_i, h_i and m_i represent the in plane hopping parameter for the i layer with $i = 0, 1$, whereas t is the out-of-plane hopping parameter. f_x with represents the function defining the first, second or

E_n	E_b	E_{ni}	g_0	h_0	m_0	g_1	h_1	m_1	t
-2.50	2.49	-6.71	-2.3	-0.1	-0.01	-3.0	0.05	0.08	-0.5

Table 4.1: DFT fitted parameters of the tight binding Hamiltonian.

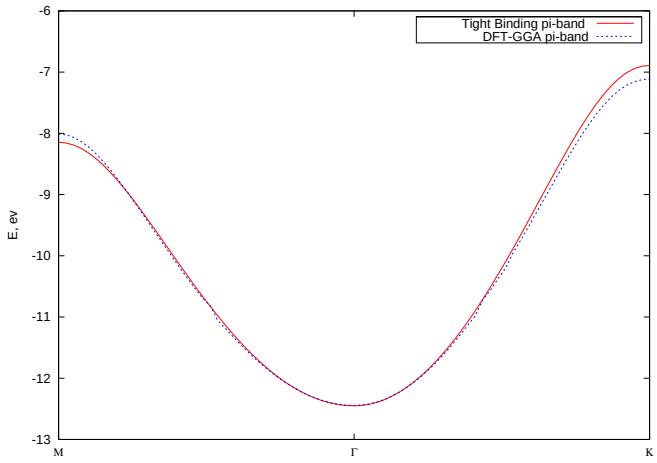

Figure 4.7: Comparison between the tight-binding pi-band of h-BN/Ni(111) (red) and the DFT one (blue).

third neighbor interaction (see 3.3.2). Note that the upper right corner of H is nothing but the 2×2 Hamiltonian of h-BN described in chapter 3.

4.3.2 Fit to the DFT band

Then we used a python code to fit the tight binding Hamiltonian to the DFT band structure. The fit is shown in figure 4.7 and the fitted parameters are reported in 4.1. The fit is not perfect at M and K, because Hamiltonian 4.1 does not account for the spin polarization which occurs at M and K as shown on figure 4.6.

Chapter 5

Electronic properties of h-BN / Au(111) and h-BN / Ir(111) interfaces

5.1 Overview

5.1.1 Crystal Structure

Like Nickel, Gold and Iridium own a cubic face centered structure. Their atomic numbers are namely 77 and 79 and then, they are also considered as transition metals. However, they exhibits different properties which imply a slightly different approach. Equally, Nickel is ferromagnetic when Gold is gyromagnetic and Iridium displays a paramagnetic nature. Thus, one can suppose that magnetic effects will not strongly impact the band structure of bare gold and iridium. The lattice parameter for bulk gold-fcc is 4.180 Å whereas the one for iridium is 3.895 Å [19]. The lattice constant of h-BN and the inter-atomic distance of metal surface do not match and this mismatch is evaluated to 12% for gold and 10% in the Iridium case. We have then incommensurate surfaces which can lead to extraordinary structure, like for instance the famous boron nitride 'nanomesh' which occurs when h-BN stands on $Rh(111)$ [20]. Up to my knowledge, no experiments have reported such patterns with h-BN on gold or iridium but we can expect that h-BN will behave on the same manner than graphene over those metals. According to references [21, 22], the graphene layer is periodically corrugated on such metals yielding Moire patterns. The epitaxial growth of h-BN over $Ir(111)$ made by Orlando and al[23] seems to confirm this position.

5.1.2 Structure models

In order to be commensurate, the h-BN/$Au(111)$ consists of a 9×9 super-cell of h-BN on top of a 8×8 super-cell of Au(111). In the same manner, the super-cell for iridium is a 11×11 cell of h-BN over a 10×10 cell of Ir(111). Even with a few layer of metal, the number of atoms increase quickly and easily gets over 1000 atoms per cell. Such sizes ask for

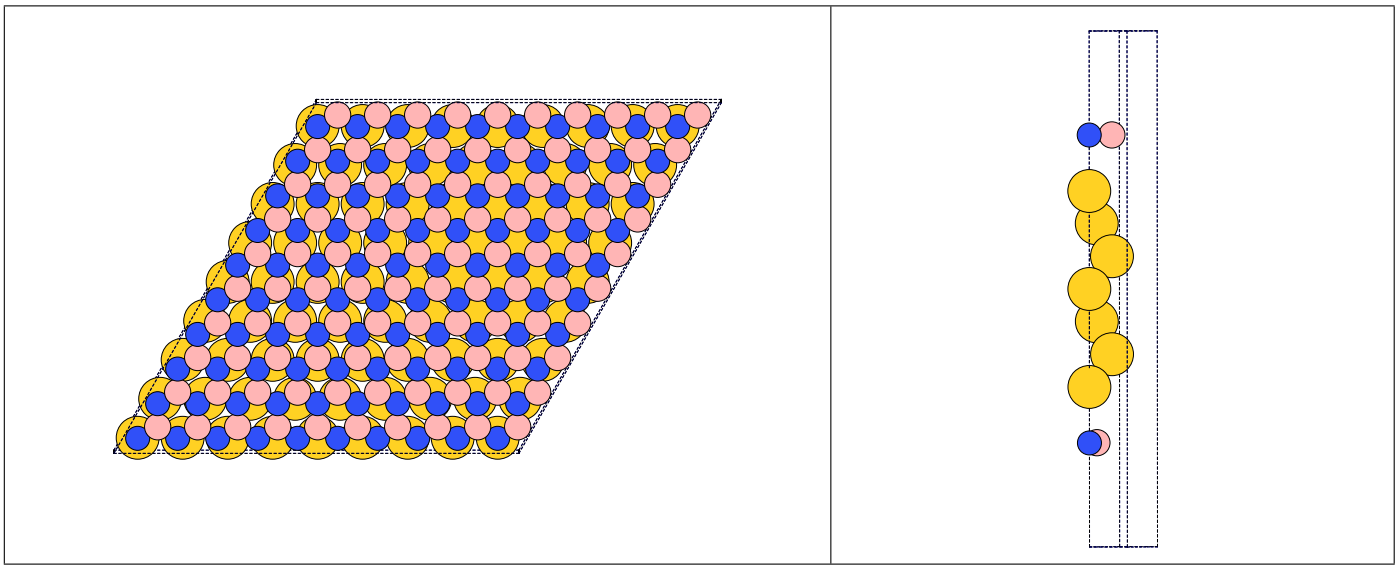

Figure 5.1: (left) Super-cell structure of 9×9 h-BN over 8×8 Au(111). (right) 1×1 cell used in the approximation.

large computational resources and then we approximated most of our calculations by using a simple 1×1 structure. This approximation strategy has already been employed so far, for the isostructural case of graphene on top of metals [24], [25], [26]. We have either to stretch h-BN or compress the metals to make them commensurate. Both configuration have been investigated and will be discussed later on.

5.1.3 Structure Optimization

As for nickel, there are six configurations the adsorption of the BN layer on top of a fcc(111) structure, with each boron and nitrogen atom able to occupy three positions (cf Fig4.2). As we forced the structure to be a 1×1 we may reasonably expect that the most energetically favorable position will be the same than reported in Sec. 4.1.2. This is confirmed by the total energy calculations depicted in Fig. 5.2. However, it is worth noting that with the super-cell structure, the configuration with N on top of atoms of the first metallic layer and B on hollow site is obviously not the only one, as Moire pattern occurs [27].

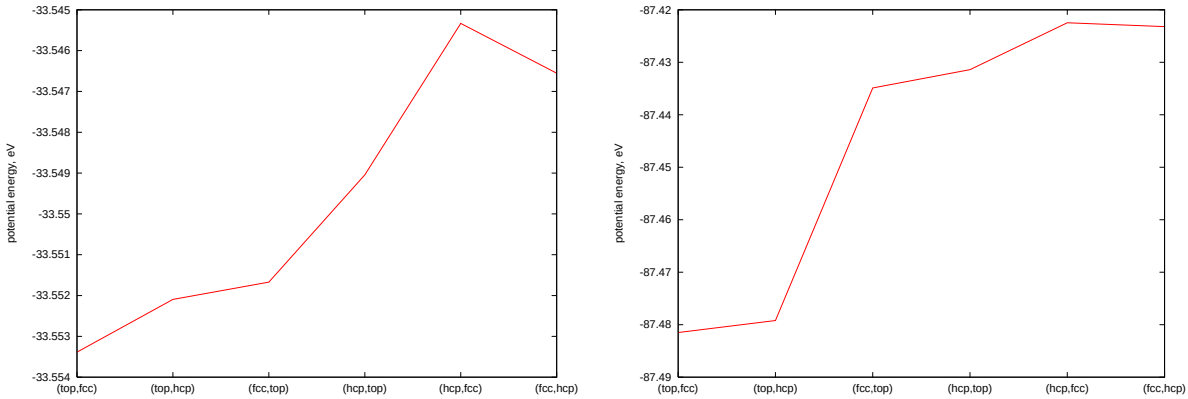

Figure 5.2: (left) Potential energy of h-BN over seven layers of $Au(111)$. On the x-axis are labeled the six possible configurations, the first part of the parentheses labeling the nitrogen atom and the other, the boron atom.(right) Potential energy of h-BN over seven layers of $Ir(111)$

As no one has reported the distance between h-BN/$Au(111)$ over gold and iridium, we also made theoretical calculations in order to have an idea of what it could be. We processed as follows: for different distances we placed h-BN over four metallic layers and computed the potential energy using a Van Der Waals exchange correlation potential. The optimal distance is then the most energetically favorable. Figure 5.3 reports the different distances and we found that the distance between h-BN and gold was of 3.5 Å and the distance between h-BN and $Ir(111)$ was 2.44 Å. As a comparison the average distance between graphene and gold – calculated with van der Waals density functional– is 3.55 Å [24] and the one between graphene and iridium is 2.3 Å [26].

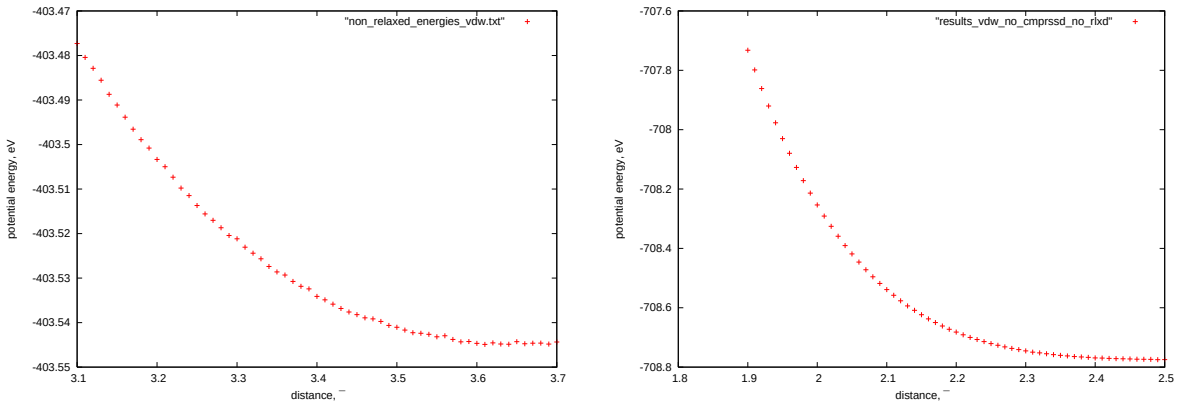

Figure 5.3: (left) Potential energy of h-BN/$Au(111)$ as a function of the distance between the two materials. (right) Potential energy of h-BN/$Ir(111)$. Energies have been computed using the van der Waals density functional (vdW-DF)

5.2 Electronic Structure

In this section we report the results of our DFT analysis and compare them with experimental ARPES data. The methodology used for DFT has been described in Sec. 3.4.1

5.2.1 Band structure of h-BN/Au(111)

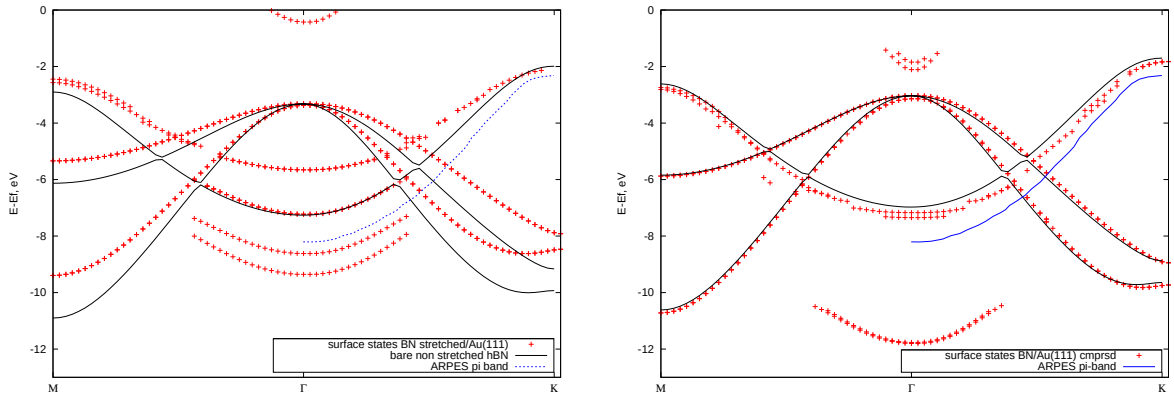

Figure 5.4: (right) Band structure of stretched h-BN over Au(111) (red) compared to the valence bands of non extended pristine h-BN/ (black) and the ARPES π-band (blue) . The k-path follows the direction $M \rightarrow \Gamma$ then $\Gamma \rightarrow K$.(right) Comparison between theoretical valence band for pristine h-BN(black) and h-BN/ over compressed Au(111) (red). The ARPES π-band is also plotted (blue)

Figure 5.4, represents the band structure of h-BN on Au(111) when the lattice parameter of h-BN is stretched to the inter-atomic distance of Au(111). In the same manner than in Chap. 4, the surface states has been added in order to compare the theoretical band structure to the experimental one. At first sight, the *pi*-band of hBN over Au simply does not match with either the theoretical π band of pristine hBN or the experimental band. Which lead us to infer than the approximation with extended h-BN is not valid. However when we compress the gold in order to get the two materials totally commensurate as it is reported on the right part of Fig. 5.4. Table 5.1 reports that the bandwidth of the theoretical *pi*-band has the same order of magnitude of the experimental ARPES band. We can then conclude than compressing gold doesn't strongly impact the band structure.

	Γ	K	Bdwth
ARPES π-band	-8.20	-2.31	5.89
DFT π-band	-6.96	-1.69	5.27
δ			0.62
DFT π-band (smll distance)	-8.20	-2.31	5.89
δ			0.00

Table 5.1: Comparison between the bandwidth of theoretical π-band and the experimental one. Values are reported in eV. The bandwidth represents the difference between the band energy at K and at Γ. Bottom lines report the same comparison but with a reduced distance between the two surface materials.

Then we compared the DFT theoretical pi-band of h-BN/$Au(111)$ with the one of pristine h-BN. Values at high-symmetry points are reported in table 5.2.

	M	Γ	K
h-BN	-2.60	-6.96	-1.69
h-BN/$Au(111)$ (top)	-2.74	-7.17	-1.82
h-BN/$Au(111)$ (bottom)	-2.81	-7.35	-1.84
$\delta 1$	0.14	0.21	0.13
$\delta 2$	0.21	0.39	0.15

Table 5.2: π band parameters for h-BN/$Au(111)$ compressed and a bare layer of h-BN at high symmetry points. Energies value are given in eV.$\delta 1$, $\delta 2$ give the difference between the h-BN band and the two hybridized value of the h-BN/$Au(111)$ pi-band. Bands for h-BN have been shifted to the Fermi level of h-BN/Au thus value are not significant.

And the right part of Fig. 5.4 shows a general view of the valence bands. It clearly shows that the electronic structure of h-BN is not impacted when h-BN stands over gold. Nevertheless, we can denote a small shift of the π-band. It is meaningful to assume that this shift comes from our approximation. Indeed we didn't take into account either the corrugation and the incommensurability of the substrate. Finally we noticed than when we reduced the distance between gold substrate and h-BN we were able to get an even better fit of the theoretical bandwidth to the experimental one. It is also reported in table 5.1 and we can then conclude that the distance between the two layers is in reality smaller than that one we got by theoretical calculation. The distance is reduced from 3.5 Å to 3.1 Å. This can be explained by reference [24] who has shown that the van Der Waals density functional may have difficulty in describing systems were mixed bonding are used (here van der waals and covalent bonding). Indeed they found a inter-layer distance between nickel(111) and graphene of 3.5 Å whereas the well-famous and experimentally corroborated distance is 2.1 Å.

	Γ	K	Bdwdth
pristine h-BN	-7.64	-2.37	5.27
ARPES	-8.23	-2.59	5.64
h-BN/Ir(111)	-9.6	-4.77	4.83

Table 5.3: Energies of the π-band for the different configurations at the symmetry points Γ and K.

5.2.2 Band structure of h-BN/Ir(111)

The electronic band structure of h-BN/Ir(111) has been calculated following the same strategy outlined in the two previous cases. We used a grid spacing of 0.16 Å in the z direction and 0.13 Å along the x, y directions. Wave functions are represented on a $17 \times 17 \times 1$ grid. The unit cell is composed of one layer of h-BN on each sides of a iridium(111) slab made of seven atomic layers. 15 Å in the z-direction is the standard amount of vacuum used to avoid interaction between replica. Table 5.3 contains the different bandwidths of the *pi*-bands for

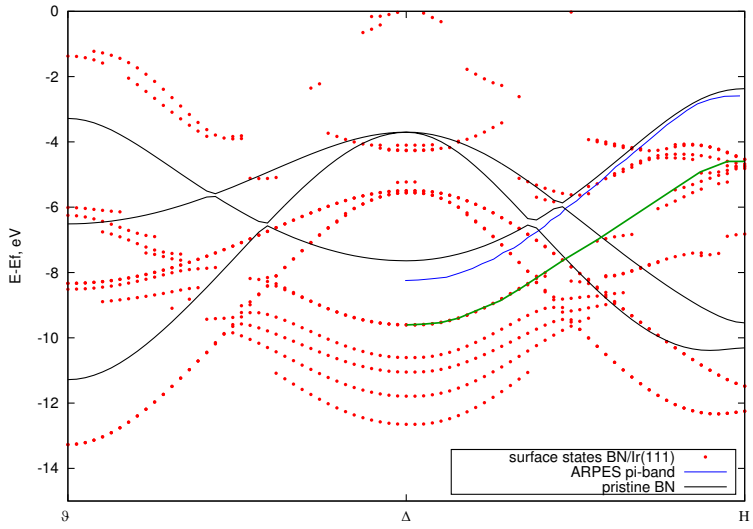

Figure 5.5: Comparison between theoretical surface states for h-BN/Ir(111) and the ARPES experiment (blue). The valence bands of pristine h-BN are plotted in black. In green the theoretical π-band is highlighted.

namely, pristine h-BN, ARPES and theoretical band for h-BN/Ir(111). The corresponding band structures are plotted in Fig. 5.5. First it is important to note than despite a very selective cutoff (0.66), surface states are numerous and not only attributed to hexagonal BN. One can, for instance, recognize that the d states of Iridium appear at the high symmetry point K. In order to bring some clarity, the DFT theoretical π-band for h-BN/Ir(111) has been highlighted in green. However, it is rather obvious that our results are far from the

ARPES *pi*-band (blue). The fact that there are possible interactions between the iridium *d* bands and the BN *pi*-band, which goes in the opposite sense of what is expected, and the significant difference in bandwidth between our theoretical data and the experiment, lead us to think that the distance of 2.44 Å between nickel and boron nitride is wrong. In Sec. 5.2.1 we noticed than despite a theoretical distance of 3.5 Å between *h*-BN and Au(111), the real one would be more likely equal to 3.1 Å. It is then consistent to say, that something went wrong with our utilization of Van der Waals density functional to evaluate the distance between the two materials. This is from where our investigations have to start in order to solve that problem. However, we can point out that there are not so many differences between the band of pristine *h*-BN and the ARPES band, one can then expect that the states of *h*-BN/ are not impacted by the presence of Iridium. Sadly, this is not what our calculation shows.

Conclusion

Work To sum up this work, we studied the electronic properties of hexagonal boron nitride on top of transition metals. The initial aim was to compare experimental band structures to theoretical ones. For that we used the Density Functional Theory implemented in the code GPAW and compared our results with an ARPES data set including electronic structures of h-BN over three different metals in the configuration (111). For h-BN we observed in the both cases, experiment and theory, a sensible decrease of around $1.2eV$ of the π-band. Since it is the principal band responsible of the electronic effects in hexagonal materials, we stated than the insulating nature of h-BN over Ni is not canceled, even enhanced. For Gold and Iridium we got into more difficulties. The theoretical $pi-band$ does not fit perfectly with the ARPES one but nonetheless, the bandwidth of both results are in the same range. We interpreted this saying that gold does not impact the band structure of hexagonal BN. We associated the mismatch between our theoretical bands and the experiment to the approximation that we made, ie a flat layer of h-BN over compressed gold. finally with the case of Iridium, we assume that something went wrong with our calculation because they clearly show a strong interaction between Iridium d bands and the pi band of hBN. The most likely hypothesis is that the too materials are closer in our calculation than in reality.

Personal On a personal plan, I learned a lot during these six months. I really improved my background in theoretical physics and now, I have a better overview of DFT. However I am well aware that there are still many open questions about my work. I think that we should do a better use of the Tight Binding theory since we achieved a nice script with Python. About the problem with Iridium, it is a pity that I could not fix the problem in time but, luckily, I have the opportunity to continue that project and I am very excited about this. I hope, for me and my supervisors, as well for the Gruneis's team who made the experiments, that we could get a nice publication by the end of the year.

Bibliography

[1] K. S. Novoselov, A. K. Geim, S. V. Morozov, D. Jiang, Y. Zhang, S. V. Dubonos, I. V. Grigorieva, and A. A. Firsov. Electric field effect in atomically thin carbon films. *Science*, 306(5696):666–669, 2004.

[2] Nasreen G. Chopra, R. J. Luyken, K. Cherrey, Vincent H. Crespi, Marvin L. Cohen, Steven G. Louie, and A. Zettl. Boron nitride nanotubes. *Science*, 269(5226):966–967, 1995.

[3] C. R. Dean, A. F. Young, I. Meric, C. Lee, L. Wang, S. Sorgenfrei, K. Watanabe, T. Taniguchi, P. Kim, K. L. Shepard, and J. Hone. Boron nitride substrates for high-quality graphene electronics. *Nature Nanotechnology*, 5:722–726, 2010.

[4] G. B. Grad, P. Blaha, K. Schwarz, W. Auwärter, and T. Greber. Density functional theory investigation of the geometric and spintronic structure of h -bn/ni(111) in view of photoemission and stm experiments. *Phys. Rev. B*, 68:085404, Aug 2003.

[5] John P. Perdew, Kieron Burke, and Matthias Ernzerhof. Generalized gradient approximation made simple. *Phys. Rev. Lett.*, 77:3865–3868, Oct 1996.

[6] P. Hohenberg and W. Kohn. Inhomogeneous electron gas. *Phys. Rev.*, 136:B864–B871, Nov 1964.

[7] Andrea Damascelli. Probing the electronic structure of complex systems by arpes. *Physica Scripta*, 2004(T109):61, 2004.

[8] D. Golberg, Y. Bando, C. C. Tang, and C. Y. Zhi. Boron nitride nanotubes. *Advanced Materials*, 19(18):2413–2432, 2007.

[9] S. Reich, J. Maultzsch, C. Thomsen, and P. Ordejón. Tight-binding description of graphene. *Phys. Rev. B*, 66:035412, Jul 2002.

[10] R. Saito, G. Dresselhaus, and M. S. Dresselhaus. *Physical Properties of Carbon Nanotubes*. Imperial, London, 1998.

[11] R. M. Ribeiro and N. M. R. Peres. Stability of boron nitride bilayers: Ground-state energies, interlayer distances, and tight-binding description. *Phys. Rev. B*, 83:235312, Jun 2011.

[12] A. Grüneis, C. Attaccalite, L. Wirtz, H. Shiozawa, R. Saito, T. Pichler, and A. Rubio. Tight-binding description of the quasiparticle dispersion of graphite and few-layer graphene. *Phys. Rev. B*, 78:205425, Nov 2008.

[13] J. J. Mortensen, L. B. Hansen, and K. W. Jacobsen. Real-space grid implementation of the projector augmented wave method. *Phys. Rev. B*, 71:035109, Jan 2005.

[14] J. Sławińska, I. Zasada, and Z. Klusek. Energy gap tuning in graphene on hexagonal boron nitride bilayer system. *Phys. Rev. B*, 81:155433, Apr 2010.

[15] Gamou Yasuo, Terai Masayuki, Nagashima Ayato, and Oshima Chuhei. Atomic structural analysis of a monolayer epitaxial film of hexagonal boron nitride/ni(111) studied by leed intensity analysis(interfaces by various techniques). *Science reports of the Research Institutes, Tohoku University. Ser. A, Physics, chemistry and metallurgy*, 44(2):211–214, 1997-03-31.

[16] W. Auwärter, T.J. Kreutz, T. Greber, and J. Osterwalder. Xpd and stm investigation of hexagonal boron nitride on ni(111). *Surface Science*, 429(1–3):229 – 236, 1999.

[17] M. N. Huda and Leonard Kleinman. *h*-BN monolayer adsorption on the Ni (111) surface: A density functional study. *Phys. Rev. B*, 74:075418, Aug 2006.

[18] V. Despoja, D. J. Mowbray, and V. M. Silkin. Tuning $mgb_2(0001)$ surface states through surface termination. *Phys. Rev. B*, 84:104514, Sep 2011.

[19] Fabien Tran, Robert Laskowski, Peter Blaha, and Karlheinz Schwarz. Performance on molecules, surfaces, and solids of the wu-cohen gga exchange-correlation energy functional. *Phys. Rev. B*, 75:115131, Mar 2007.

[20] Martina Corso, Willi Auwärter, Matthias Muntwiler, Anna Tamai, Thomas Greber, and Jürg Osterwalder. Boron nitride nanomesh. *Science*, 303(5655):217–220, 2004.

[21] Shu Nie, Norman C. Bartelt, Joseph M. Wofford, Oscar D. Dubon, Kevin F. McCarty, and Konrad Thürmer. Scanning tunneling microscopy study of graphene on au(111): Growth mechanisms and substrate interactions. *Phys. Rev. B*, 85:205406, May 2012.

[22] Alpha T N'Diaye, Johann Coraux, Tim N Plasa, Carsten Busse, and Thomas Michely. Structure of epitaxial graphene on ir(111). *New Journal of Physics*, 10(4):043033, 2008.

[23] Fabrizio Orlando, Rosanna Larciprete, Paolo Lacovig, Ilan Boscarato, Alessandro Baraldi, and Silvano Lizzit. Epitaxial growth of hexagonal boron nitride on ir(111). *The Journal of Physical Chemistry C*, 116(1):157–164, 2012.

[24] M. Vanin, J. J. Mortensen, A. K. Kelkkanen, J. M. Garcia-Lastra, K. S. Thygesen, and K. W. Jacobsen. Graphene on metals: A van der waals density functional study. *Phys. Rev. B*, 81:081408, Feb 2010.

[25] G. Giovannetti, P. A. Khomyakov, G. Brocks, V. M. Karpan, J. van den Brink, and P. J. Kelly. Doping graphene with metal contacts. *Phys. Rev. Lett.*, 101:026803, Jul 2008.

[26] R Brako, D Šokčević, P Lazić, and N Atodiresei. Graphene on the ir(111) surface: from van der waals to strong bonding. *New Journal of Physics*, 12(11):113016, 2010.

[27] Hans Peter Koch, Robert Laskowski, Peter Blaha, and Karlheinz Schwarz. Adsorption of gold atoms on the *h*-bn/rh(111) nanomesh. *Phys. Rev. B*, 84:245410, Dec 2011.